

A possible wave-optical effect in lensed FRBs

Goureesankar Sathyanathan^{1,2}, Calvin Leung³, Olaf Wucknitz⁴ and Prasenjit Saha⁵,

¹ Indian Institute of Science Education and Research Thiruvananthapuram 69551, Kerala, India
e-mail: gouree.sath@gmail.com

² Department of Physics and Astronomy, University of California, Riverside, CA 92521, USA

³ Department of Astronomy, University of California Berkeley, Berkeley, CA 94720, USA

⁴ Max-Planck-Institut für Radioastronomie, Auf dem Hügel 69, 53121 Bonn, Germany

⁵ Physik-Institut, University of Zurich, Winterthurerstrasse 190, 8057 Zurich, Switzerland
e-mail: psaha@physik.uzh.ch

March 3, 2026

ABSTRACT

Context. Fast Radio Bursts (FRBs) are enigmatic extragalactic bursts whose properties are still largely unknown, but based on their extremely small time duration, they are proposed to have a compact structure, making them candidates for wave-optical effects if gravitational lensed. If an FRB is lensed into multiple-images bursts at different times by a galaxy or cluster, a likely scenario is that only one image is detected, because the others fall outside the survey area and time frame.

Aims. In this work we explore the FRB analog of quasar microlensing, namely the collective microlensing by stars in the lensing galaxy, now with wave optics included. The eikonal regime is applicable here.

Methods. We study the voltage (rather than the intensity) in a simple simulation consisting of (a) microlensing stars, and (b) plasma scattering by a turbulent interstellar medium.

Results. The auto-correlation of the voltage shows peaks (at order-microsecond separations) corresponding to wave-optical interference between lensed micro-images. The peaks are frequency dependent if plasma-scattering is significant. While qualitative and still in need of more realistic simulations, the results suggest that a strongly-lensed FRB could be identified from a single image.

Conclusions. Microlensing could sniff out macro-lensed FRBs.

Key words. fast radio bursts – strong lensing

1. Introduction

Ever since the discovery of an unprecedented signal in an archival radio time series by D. J. Narkevic, then an undergraduate researcher, and the interpretation of that signal as an exceptionally bright extragalactic radio transient (Lorimer et al. 2007), Fast Radio Bursts (FRBs) have steadily increased in interest (Ng 2023; Lorimer et al. 2024).

FRBs last from microseconds to milliseconds, and are characterized by very high dispersion measures indicating cosmological distances, which implies that they are 10 to 12 orders of magnitude brighter than radio sources within the Milky Way. Also, they are very common across the sky, with a FRB expected once every ten seconds (Keane & Petroff 2015; Champion et al. 2016). While early single-dish telescopes like Parkes and Arecibo could detect only a few FRBs, the CHIME telescope (CHIME/FRB Collaboration et al. 2018) with its much larger field of view has detected hundreds (CHIME/FRB Collaboration et al. 2021). Observation of additional signals from FRB121102 led to the understanding that FRBs can be of a repeating nature (Spitler et al. 2014, 2016), showing that they are not always cataclysmic events. While follow-up observations with single-dish telescopes were difficult, CHIME has reported that around 10% of FRBs detected have a repeating feature (Andersen et al. 2020; Andersen et al. 2023), and a subset of those have periodic activity windows. Repeating FRBs have wide-ranging properties, peaking at different frequencies, with the presence of multiple components (e.g., Chatterjee et al. 2017; Tendulkar et al. 2017).

In many cases, precise localization can be carried out, and in these cases, the studies of the intergalactic medium are possible.

The rapid time variation in FRBs indicates small intrinsic sizes. This would imply that FRB signals are spatially coherent, which would lead to interference effects in cases of gravitational lensing. Several authors (Eichler 2017; Katz et al. 2020; Kader et al. 2022; Leung et al. 2022; Kumar & Beniamini 2023) have considered the possible lensing of FRBs by black holes or other compact masses. These works also note a significant complication, which is frequency dependent plasma lensing by the interstellar medium in the host galaxy and in the Milky Way.

Wucknitz et al. (2021) consider multiple images in galaxy and cluster lensing, and draw attention to the prospect of measuring redshift drift if time delays from FRB repeaters are observed. One of the potential complications noted in that work is the collective microlensing by stars in the lensing galaxy or cluster. Lewis (2020) studied the expected effect of microlensing on lensing time delays. A difficulty in finding such multiple-image systems is that a survey may detect one image from a system, but miss the others because the survey pointing has moved to a different part of the sky. Since of order one in a thousand high-redshift objects is lensed into multiple images, it is plausible that a strongly-lensed FRB has already been observed without being recognisable as such.

In this work we carry out some simple simulations of wave optics in collective microlensing by stars. That is, we combine ideas from the works mentioned in the previous two paragraphs. The result suggests that collective microlensing by stars imprints

an observable signature on a lensed FRB, even without having to detect more than one image.

2. Gravitational lensing with eikonal optics

The formation of multiple images of a source by an intervening gravitational field, commonly called strong lensing, occurs in two very different regimes. One involves stellar or planetary-scale masses in or near the Milky Way (see e.g., Mróz et al. 2024). The other is over cosmological distances and is the situation more relevant to FRBs. The theory is introduced in several places, such as Meneghetti (2022) and Saha et al. (2024) in recent years, with Leung et al. (2023) covering the wave optics part in detail. We summarise the essential points below.

2.1. Images and magnification

Strong lensing involves a combination of two very different scales. One is of distances in the combination

$$\mathcal{D} \equiv \frac{D_d D_s}{D_{ds}} \quad (1)$$

Here D_d and D_s are angular-diameter distances from the observer to the deflector (lens) and the source respectively, and D_{ds} is the angular-diameter distance from the deflector to the source. \mathcal{D}/c is of order the total light travel time. A second scale is

$$\mathcal{T} \equiv \frac{4GM}{c^3} \quad (2)$$

which is always $\ll \mathcal{D}/c$. Image separations are on the scale of the Einstein radius, given by

$$\theta_E^2 = \frac{c\mathcal{T}}{\mathcal{D}} \quad (3)$$

\mathcal{T} itself turns out to be the typical difference in light travel time between images, known as time delays. For multiple images to form θ_E needs to fit within the angular size of the mass itself. This becomes more common for larger distances because $\theta_E \propto \mathcal{D}^{-1/2}$ whereas angular size $\propto \mathcal{D}_d^{-1}$.

There are separated subfields of lensing, corresponding to different scales of \mathcal{T} and θ_E .

- For cluster lenses (for a recent review see Natarajan et al. 2024) where \mathcal{T} is years to decades, and θ_E reaches the arc-minute scale.
- For galaxy lenses (see Shajib et al. 2024, for a recent review) \mathcal{T} is days to months, while θ_E is arc-second scale.
- Third is the collective lensing by stars within a strongly-lensing galaxy or cluster, which splits the individual images formed (the so-called macro-images) into many micro-images. Here \mathcal{T} is of microsecond scale and θ_E is of micro-arcsecond scale. The phenomenon is of interest for sources that are small enough, and has been extensively studied for lensed quasars (see e.g., Vernardos et al. 2024). The scale of θ_E is too small to resolve the images, but changes in brightness resulting from transverse motion is observable. It is potentially even more interesting for FRBs, because of the smaller source size.

Lensing often uses the arrival time surface. Consider the possible light travel time for a photon originating at angular position β , getting deflected and then arriving from direction θ . The arrival time can be scaled to a dimensionless form as

$$t(\theta; \beta) = (1 + z_d)(\mathcal{D}/c) \tau(\theta; \beta) \quad (4)$$

and expressed as the sum of geometric and gravitational delays. For a single point mass the dimensionless arrival time is

$$\tau(\theta; \beta) = \frac{1}{2}|\theta - \beta|^2 - \theta_E^2 \ln|\theta - \theta_0| \quad (5)$$

Contributions for more masses can be summed or integrated. For collective microlensing by N equal masses we have

$$\tau(\theta; \beta) = \frac{1}{2}|\theta - \beta|^2 - \psi_B(\theta) - \theta_E^2 \sum_{i=1}^N \ln|\theta - \theta_i| \quad (6)$$

with ψ_B representing a background contribution due to all other masses. By Fermat's principle, images form where

$$\nabla\tau(\theta) = 0 \quad (7)$$

gives the lens equation

$$\beta = \theta - \nabla\psi_B(\theta) - \theta_E^2 \sum_{i=1}^N \frac{\theta - \theta_i}{|\theta - \theta_i|^2} \quad (8)$$

The deflection of light rays by large-scale gravitational lenses like galaxies or galaxy-clusters is described by the macrolensing potential, denoted by $\psi_B(\theta)$ in Eq. (8). The macrolensing potential governs the overall distortion of light rays originating from background sources. The deflection angle at angular position θ in the sky is given by the gradient of the potential, $\nabla\psi_B(\theta)$. A Taylor expansion of the deflection angle yields, at leading order, a constant term corresponding to an effective shift in the apparent source position from β . The next-order term, involving the second derivative of the potential (or the first derivative of the deflection angle), captures the local stretching and shearing of the arrival-time surfaces. Microlensing simulations (going back to Paczynski 1986) generally assume constant stretching and shearing, neglecting higher-order effects. For simpler simulations designed for illustrative purposes (e.g., Vernardos et al. 2024) the background potential may be neglected altogether. Its omission does not qualitatively affect our primary results.

By visualizing the arrival-time surfaces $\tau(\theta; \beta)$ it is possible to visualize three kinds of images formed at locations where the surface has zero gradient. If there is no lens, then there is a minimum at the point $\theta = \beta$ surrounded by a parabolic well. A circular lens directly aligned with the source replaces this parabola with a hill surrounded by a circular valley. However, if this is not the case, the valley will be asymmetric with a bowl on one side. The more complex the mass distribution, the more valleys and hills appear, leading to maxima and minima. Another set of images is formed by saddle points that also satisfy the zero-gradient condition.

The Hessian of $\tau(\theta)$ determines how quickly or slowly we will be moved off-source by a change in θ . By defining $(M^{-1})_{ij} \equiv \partial_i \partial_j \tau(\theta)$ as the inverse magnification matrix, it can explain the lensing caused by many small and finite sources as

$$\Delta\theta_i = \sum_j \partial_i \partial_j \tau(\theta) \Delta\beta_j \quad (9)$$

The scalar magnification $\mu(\theta)$ is given by

$$1/\mu(\theta) = \det(\partial_i \partial_j \tau(\theta)) \quad (10)$$

Note that the magnification is negative for images at saddle points.

2.2. Wave optics in the eikonal regime

While geometric optics is a good enough approximation for most astronomical sources that are large enough so radiation from different parts of the source reaches the observer incoherently, wave optics applies to small and far away sources. This applies to gravitational waves (e.g., Dai et al. 2020; Mishra et al. 2021). The case of FRBs is actually simpler, because of the much higher frequencies, enabling an eikonal approximation.

An unlensed narrow-band signal of the form

$$S_{UL} = \sum_{\nu} S(\nu) \exp(2\pi i \nu t) \quad (11)$$

results in a lensed signal

$$S_L = \sum_{\nu} A(\nu) S(\nu) \exp(2\pi i \nu t) \quad (12)$$

where we have defined

$$A(\nu) = \sum_k \alpha_k \exp(2\pi i \nu \tau_k) \quad (13)$$

$$\alpha_k = |\mu_k|^{1/2} \times \begin{cases} 1 & \text{for minima} \\ i & \text{for saddle points} \\ -1 & \text{for maxima} \end{cases} \quad (14)$$

and τ_k corresponds to the k -th micro-image. The lensed signal from a large number of micro-images is thus straightforward to calculate.

2.3. Plasma scattering

In addition to gravitational lensing, an important obstacle in the radio domain is the scattering caused by turbulence of the interstellar medium. This depends on the electron density and amounts to an additional time delay that is proportional to ν^{-2} . This produces deflections similar to those produced by microlensing, forming a large number of images that can interfere with each other. Due to their extragalactic nature, FRBs can be affected by scattering in the lens galaxy and the intergalactic medium apart from the Milky Way. This would be most serious if the lensing galaxy is gas-rich, but as most lensing galaxies are elliptical, a comparatively low level of plasma scattering is expected (Wucknitz et al. 2021).

To model plasma scattering we add a term

$$(\nu_0/\nu)^2 \theta_E^2 p(\theta) \quad (15)$$

to the scaled time-delay (6). Here $p(\theta)$ denotes a turbulent field normalized as

$$\langle p^2(\theta) \rangle = 1 \quad (16)$$

The strength is then set by ν_0 , which we can understand as the frequency for which plasma scattering contributes as much as a star microlensing on its own. Gravitational lensing dominates in the $\nu \gg \nu_0$ regime. Plasma scattering becomes less and less important with an increase in ν .

To produce a realization of $p(\theta)$ we let its Fourier transform be a power law with small-scale and large-scale cutoffs (cf. Eq. 1 in Armstrong et al. 1995). The Fourier component corresponding to

$$(q_x, q_y, q_z) \quad (17)$$

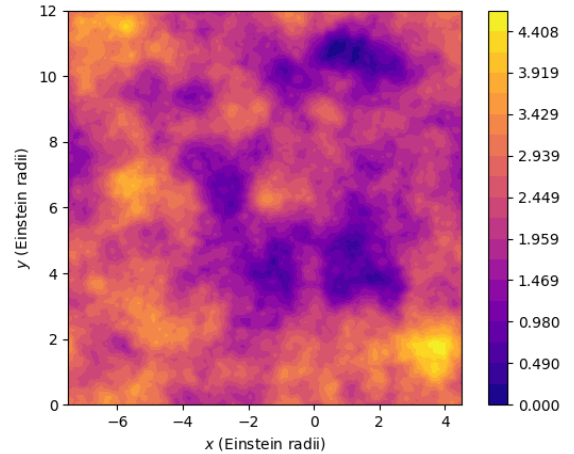


Fig. 1. Illustration of time delay due to turbulent ISM, normalized according to Eq. (16). The spatial scale is the same as the microlensing fields in left panels in Figs. 2–4 below.

is given an amplitude of

$$(q^2 + L_0^{-2})^{-11/6} \exp\left(-\frac{1}{2} l_0^2 q^2\right) \quad (18)$$

and a random phase. Here l_0 and L_0 are the grid-size and field-size respectively, which act as the small-scale and large-scale cutoffs. Since an integral along the line of sight is desired, we put $q_z = 0$. The real part of $p(\theta)$ is taken, and normalized according to Eq. (16). Fig. 1 shows an example realization of $p(\theta)$.

The grid-size for the simulation is chosen as 1024×1024 , with each point corresponding to one Einstein radius. The physical distance corresponding to the Einstein radius (Eq. 3) is given by

$$\mathcal{D}\theta_E = \sqrt{c\mathcal{T}\mathcal{D}} \quad (19)$$

and is of order milli-parsec or light-days. The small-scale cutoff l_0 is roughly $10^{-2} \mathcal{D}\theta_E$ and the large-scale cutoff L_0 corresponds to $10 \mathcal{D}\theta_E$. The region of interest where microlensing is assumed to take place lies between these two scales, and the turbulence is expected to be scale-free.

3. A simple simulation

We present in this section the results obtained from the effects of macrolensing, microlensing, and a turbulent interstellar plasma on the FRB signal.

We start with illustrative microlensing simulation from the recent literature (Vernardos et al. 2024, —see especially their Figs. 4 and 6). The simulation has 50 equal point-mass lenses, whose Einstein radii cover $\sim 40\%$ of the image plane ($\kappa_* \sim 0.4$ in the usual notation). This assumes that the stellar mass is a significant contributor to the total lensing mass, but the stellar mass need not be dominant. More elaborate simulations have many thousands of particles, and include a smooth tidal field (known as external shear), but the qualitative properties of micro-images are already present in this example. Of particular interest is a cluster of four bright micro-images, two minima and two saddle points.

To the scaled time delay (6) corresponding to the above lensing system, we add the plasma scattering term (15) with adjustable ν_0 . The micro-images are found using a simple recursive

grid search. A random coherent signal spectrum $S(\nu)$ is generated and this signal is lensed according to Eqs. (12–14). The lensed signal is then auto-correlated. Using Eqs. (12–14), the auto-correlation turns out to be

$$C(t) = \int S_L(t') S_L^*(t' - t) dt' \\ = \sum_{\nu} \sum_{j,k} \alpha_j \alpha_k^* |S(\nu)|^2 \exp(2\pi i \nu (t + \tau_j - \tau_k)) \quad (20)$$

$C(t)$ clearly has peaks when $t = \tau_k - \tau_j$. For a theoretical understanding, we distinguish between the real and imaginary parts of the auto-correlation, even though they may not be distinguishable in practice.

3.1. Lensing-dominated regime

Fig. 2 illustrates this regime. The left panel in Fig. 2 is equivalent to Fig. 6 (up to some cosmetics) in Vernardos et al. (2024). The micro-images present are as follows.

- Two bright minima with time delays (say) τ_0, τ_1 .
- Two bright saddle points with τ_2, τ_3 .
- Faint saddle points with $\tau_4, \tau_5, \tau_6 \dots$

An important property of collective microlensing by stars (see e.g., Nityananda & Ostriker 1984; Saha & Williams 2011) is that the observable signal is completely dominated by a few bright micro-images, while the faint micro-images, though much more numerous, have a negligible contribution to the light. In this example, the two bright minima and two bright saddle points all have $|\mu_k| \sim 1$ with the remaining images being orders of magnitude fainter. Thus only the first four micro-images would be observationally relevant. For a theoretical understanding, however, we will continue to consider the first few faint micro-images as well.

The right panel in Fig. 2 shows the auto-correlation (Eq. 20) of the lensed signal in the left panel of the same figure. Each line in the auto-correlation (after the line at zero delay) is associated with a pair of micro-images. The strong lines are associated with pairs of bright micro-images. Blue and magenta indicate the real and imaginary parts.

- At $\tau_1 - \tau_2$ between two opposite-parity images, and therefore imaginary.
- At $\tau_3 - \tau_2$ and $\tau_1 - \tau_0$ which happen to be almost equal, between like-parity images, and therefore real.
- At $\tau_2 - \tau_0$ and $\tau_3 - \tau_1$ which again happen to be nearly equal between like-parity images.
- At $\tau_3 - \tau_0$ again between opposite parity images.

Then, there is a repeating pattern of four lines, as a faint micro-image is paired with the four bright micro-images

- at $\tau_k - \tau_0$ and $\tau_k - \tau_1$ between opposite-parity images, and
- at $\tau_k - \tau_2$ and $\tau_k - \tau_3$ between like-parity images

for $k = 4, 5, 6 \dots$ which continues beyond the figure. These are only of theoretical interest, as there is no prospect of observing them. There are also some even fainter lines

- at $\tau_k - \tau_j$

for $k, j > 3$ corresponding to pairs of faint micro-saddles.

The magenta lines in Fig. 2 all happen to be negative. The reason for this can be seen by referring back to Eq. (20) for

the auto-correlation. Since the figure shows positive t , it implies $\tau_k > \tau_j$ at the peaks. The magenta lines come from cases where τ_j is a minimum and τ_k is a saddle point. Since all the saddle-points arrive later than all the minima, τ_k always corresponds to a saddle point, and the associated α_k^* factor makes the imaginary part negative. If there would be any saddle points arriving earlier than a minimum, a positive magenta line would appear.

3.2. The effect of plasma scattering

We now show the effect of adding the plasma-scattering term (15). Fig. 2 discussed above actually already had a small plasma-scattering contribution, corresponding to $\nu = 20 \nu_0$. In the next two figures, we gradually reduce ν . In these figures we also zoom in to highlight the bright micro-images and the auto-correlation peaks between them.

In Fig. 3, we see that down to $\nu = 10 \nu_0$ there is only a slight shift in the auto-correlation peaks; that is, plasma scattering is not significant. When we reduce to $\nu = 8 \nu_0$ however, a qualitative change appears. The bright micro-minimum initially at τ_2 splits into three bright micro-images (two minima and a saddle point). Accordingly, more lines appear in the auto-correlation.

In Fig. 4, the frequency is lowered in steps to $5 \nu_0$. The saddle point initially at τ_3 now splits into three images, while the triplet near τ_2 that formed at $\nu = 8 \nu_0$ separates out a little. Here we have the first example of a minimum (near τ_3) that is later than a saddle point (near τ_2), leading to a positive imaginary part.

We thus see the familiar theme, that the observable is frequency independent if gravitational lensing dominates, and frequency dependence if interaction with the medium is important.

4. Observational aspects

Details of the observations and data processing go beyond the scope of this theoretically motivated manuscript, but we need to understand the chance of an actual detection of microlensing signatures.

FRBs are basically found as peaks in time series of the detected power over long observations. In reality, the data are channelised to form dynamic (time-resolved) spectra, to be able to correct for dispersion from the interstellar medium, and to distinguish astrophysical bursts from artificial interference. For the microlensing analysis, the original voltage signal $S(t)$, or equivalently $S(\nu)$, is needed for the duration of the burst, to form the autocorrelation according to Eq. (20). Such data are now recorded on a regular basis by CHIME and ASKAP, but also by telescopes like Effelsberg, which are used for follow-up observations of repeating bursts.

Because the central peak at $C(0)$ corresponds to the integrated detected power, we know it to be well above the noise level. Microlensing-induced peaks at $\tau_k - \tau_j$ (for $k > j \geq 0$) will be proportional to $|\alpha_j \alpha_k|$ or the geometric mean of the intensities of the corresponding micro-images. This can be compared to the central peak, which is effectively proportional to $\sum_j |\alpha_j|^2$ (the sum of all intensities), after averaging over frequency.

For the image configuration in Fig. 2, the ratio is 0.29 for the highest microlensing peak compared to $C(0)$, which is detectable if the initial FRB detection has a sufficient signal-to-noise ratio. The actual detection analysis requires a thorough statistical analysis of false-detection rates, taking into account the number of trial lags.

The frequency (here ν_0) at which plasma scattering and lensing become comparable is unknown. If ν_0 is lower than the GHz

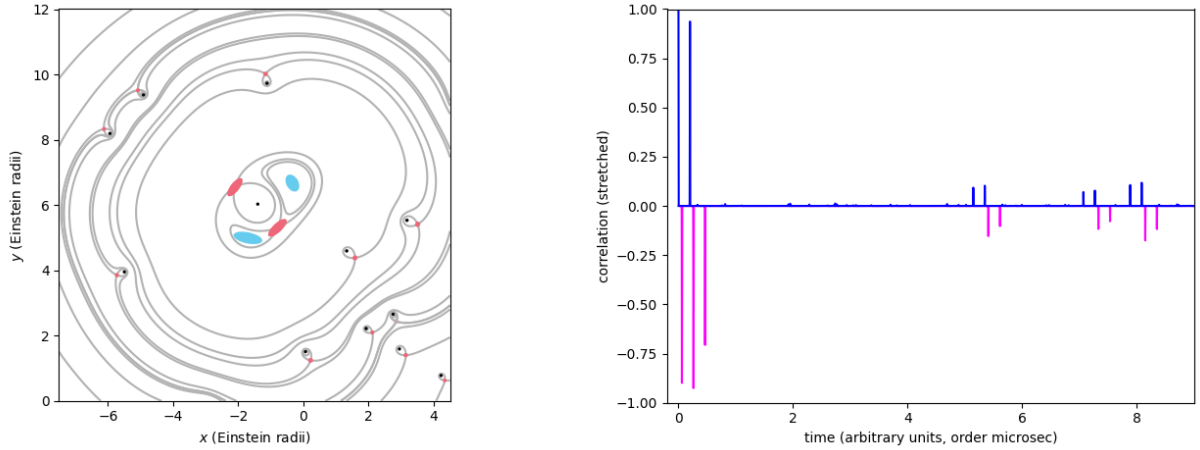


Fig. 2. *Left.* Micro-images in the lensing-dominated regime. Black dots mark stellar masses. Gray curves show arrival time contours. Ellipses are micro-images (blue for minima, red for saddle points). *Right.* Auto-correlation signals: blue for the real part, magenta for the imaginary part. A tanh activation function has been applied to reduce the contrast between the lines.

scale of FRB observations, the wave-optical effect discussed here will be observable. Otherwise the effect will be washed out by plasma scattering. The overall delay due to plasma scattering will be comparable to the observed dispersion (which is of order a second). This is vastly larger than the microsecond scale delays due to individual stars, but tiny compared to the overall time delay of to all the lensing mass (time delays in galaxy lensing are months). What is relevant is whether the plasma-scattering term varies on the microsecond scale over the transverse scale of microlensing (which is micro-arcseconds or picoradians). Equivalently, the question is whether the small-scale cutoff of the turbulent plasma is smaller than the microlensing scale.

The scattering delays can depend on the galactic latitude, with low galactic latitudes showing stronger effects in general (Wucknitz et al. 2021). For latitudes above 20° , a scattering delay at 1.4GHz is always less than 1 microsecond. Additional constraints on small-scale plasma fluctuations come from secondary-spectrum measurements (Sprenger et al. 2021, Fig. 4). Apart from a special case at 1 millisecond, most scattering features have delays of the order of a few 100 microseconds at 330MHz. As typical delays scale as $\sim \nu^{-4.4}$, even the strongest 1 millisecond feature would be ~ 1.7 microseconds at 1.4GHz - a case of strong scattering. Characteristic scattering angles at about 330MHz are also found to be ~ 30 mas, which scale with frequency as $\nu^{-2.2}$, implying angular broadening of order ~ 1 mas at 1.4GHz (Sprenger et al. 2021, Fig. 9). So, it turns out microseconds and mas are appropriate order-of-magnitude estimates at 1.4GHz. In the lensing galaxy however, scattering can be substantially stronger as the delays scale with distance. In such environments, plasma phase fluctuations may approach or exceed microlensing scales and could potentially suppress wave-optics features.

5. Conclusions

Based on the above simulation, we make the following interpretation. If a lensed FRB is smaller than the Fresnel scale — which is $(Dc/\nu)^{1/2} \sim 10$ au for GHz observations — and moreover is not smeared too much by the contents of the interstellar or intergalactic medium — making it a coherent source — then a single macro-image could be used for recognizing the lens. The well-known fine time structure in FRBs indicates that they are sufficiently small to be coherent. Since most strongly lensing

galaxies are elliptical, lensed FRBs would be exposed to the low end of plasma scattering.

It would be interesting to examine auto-correlated voltage time series at different frequencies (as simulated in Kader et al. 2024, Figs. 11–12) for a sample of FRBs observed in different parts of the sky and thus through different regions of the Milky Way. While not expected to yield any lensed specimens, even a small sample would give an indication of the importance of plasma scattering through the frequency dependence of the auto-correlation. If there are frequency-dependent peaks in the auto-correlation at all frequencies, it would not be possible to separate the contributions of gravitational lensing and plasma scattering. If auto-correlation peaks are absent at some (high) frequencies, the outlook for finding lenses by this method would be positive.

References

- Andersen, B. C., Bandura, K., Bhardwaj, M., et al. 2023, *The Astrophysical Journal*, 947, 83
- Andersen, B. C., Bandura, K. M., Bhardwaj, M., et al. 2020, *Nature*, 587, 54
- Armstrong, J. W., Rickett, B. J., & Spangler, S. R. 1995, *ApJ*, 443, 209
- Champion, D. J., Petroff, E., Kramer, M., et al. 2016, *Monthly Notices of the Royal Astronomical Society: Letters*, 460, L30–L34
- Chatterjee, S., Law, C. J., Wharton, R. S., et al. 2017, *Nature*, 541, 58–61
- CHIME/FRB Collaboration, Amiri, M., Andersen, B. C., et al. 2021, *ApJS*, 257, 59
- CHIME/FRB Collaboration, Amiri, M., Bandura, K., et al. 2018, *ApJ*, 863, 48
- Dai, L., Zackay, B., Venumadhav, T., Roulet, J., & Zaldarriaga, M. 2020, *Search for Lensed Gravitational Waves Including Morse Phase Information: An Intriguing Candidate in O2*
- Eichler, D. 2017, *The Astrophysical Journal*, 850, 159
- Kader, Z., Dobbs, M., Leung, C., Masui, K. W., & Sammons, M. W. 2024, *Phys. Rev. D*, 110, 123027
- Kader, Z., Leung, C., Dobbs, M., et al. 2022, *Phys. Rev. D*, 106, 043016
- Katz, A., Kopp, J., Sibiryakov, S., & Xue, W. 2020, *MNRAS*, 496, 564
- Keane, E. F. & Petroff, E. 2015, *Monthly Notices of the Royal Astronomical Society*, 447, 2852–2856
- Kumar, P. & Beniamini, P. 2023, *MNRAS*, 520, 247
- Leung, C., Jow, D., Saha, P., et al. 2023, *arXiv e-prints*, arXiv:2304.01202
- Leung, C., Kader, Z., Masui, K. W., et al. 2022, *Phys. Rev. D*, 106, 043017
- Lewis, G. F. 2020, *MNRAS*, 497, 1583
- Lorimer, D. R., Bailes, M., McLaughlin, M. A., Narkevic, D. J., & Crawford, F. 2007, *Science*, 318, 777
- Lorimer, D. R., McLaughlin, M. A., & Bailes, M. 2024, *Astrophysics and Space Science*, 369
- Meneghetti, M. 2022, *Introduction to Gravitational Lensing: With Python Examples*
- Mishra, A., Meena, A. K., More, A., Bose, S., & Bagla, J. S. 2021, *MNRAS*, 508, 4869

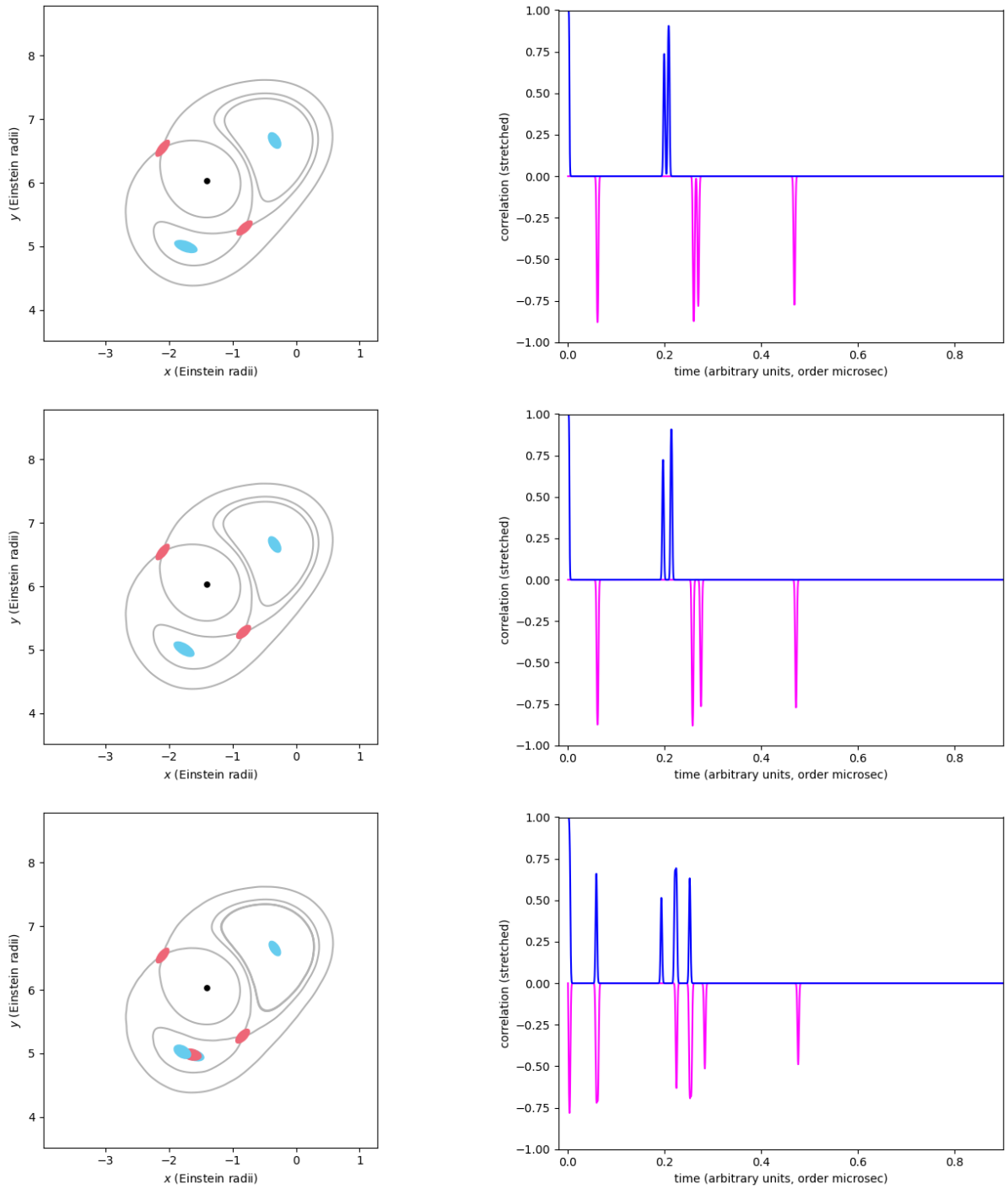


Fig. 3. Arrival time contours (left) and auto-correlation signals (right) for intermediate-frequency signals at ν/ν_0 of 13 (top row), 10 (middle row), 8 (bottom row)

Mróz, P., Udalski, A., Szymański, M. K., et al. 2024, *ApJ*, 976, L19
Natarajan, P., Williams, L. L. R., Bradač, M., et al. 2024, *Space Sci. Rev.*, 220, 19
Ng, C. 2023, A brief review on Fast Radio Bursts
Nityananda, R. & Ostriker, J. P. 1984, *Journal of Astrophysics and Astronomy*, 5, 235
Paczynski, B. 1986, *ApJ*, 301, 503
Saha, P., Sluse, D., Wagner, J., & Williams, L. L. R. 2024, *Essentials of strong gravitational lensing*
Saha, P. & Williams, L. L. R. 2011, *MNRAS*, 411, 1671
Shajib, A. J., Vernardos, G., Collett, T. E., et al. 2024, *Space Sci. Rev.*, 220, 87
Spitler, L. G., Cordes, J. M., Hessels, J. W. T., et al. 2014, *ApJ*, 790, 101
Spitler, L. G., Scholz, P., Hessels, J. W. T., et al. 2016, *Nature*, 531, 202

Sprenger, T., Wucknitz, O., Main, R., Baker, D., & Briske, W. 2021, *MNRAS*, 500, 1114
Tendulkar, S. P., Bassa, C. G., Cordes, J. M., et al. 2017, *ApJ*, 834, L7
Vernardos, G., Sluse, D., Pooley, D., et al. 2024, *Space Sci. Rev.*, 220, 14
Wucknitz, O., Spitler, L. G., & Pen, U.-L. 2021, *Astronomy & Astrophysics*, 645, A44

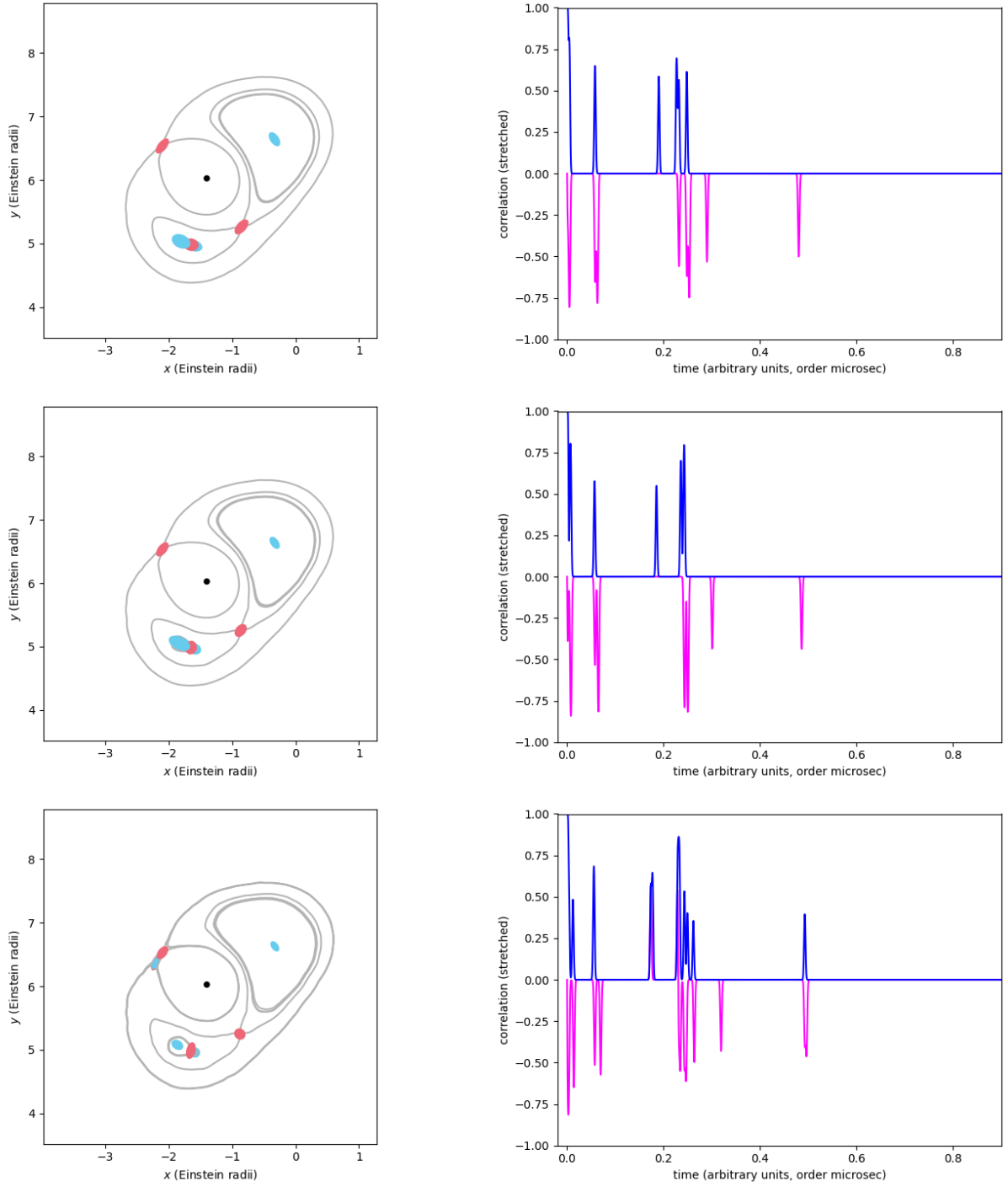


Fig. 4. Arrival time contours (left) and auto-correlation signals (right) for low-frequency signals, ν/ν_0 being 7 (top row), 6 (middle row), 5 (bottom row). The slight wiggleness of the curves in the bottom left panel are due to small-scale fluctuations from plasma scattering.